International Journal of Solids and Structures 320 (2025) 113535

Contents lists available at ScienceDirect

International Journal of Solids and Structures

journal homepage: www.elsevier.com/locate/ijsolstr

Analytical derivations for interfacial elastic deformation during the initial corrosion of metals: Thin film and thick layer implications

Asghar Aryanfar [a],*, Semih Can [b],[1], Umut Ureyen [c], William Goddard III [d]

[a] Boğaziçi University [2], Bebek, Istanbul, 34342, Turkey
[b] Texas A&M University, 400 Bizzell St, College Station, TX 77840, United States of America
[c] Politecnico di Milano, Piazza Leonardo Da Vinci 32, Milan, 20133, Italy
[d] California Institute of Technology, 1200 E California Blvd, Pasadena, CA 91125, United States of America

ARTICLE INFO

Keywords:
Interfacial deformation
Corrosion
Mismatch
Shape distortion

ABSTRACT

The corrosion of industrial components contains several attributes, mainly comprising perspectives from (electro) chemistry and physics of materials. In this work, a new solely mechanics-based constitutive paradigm is developed, which incorporates swelling-induced deformation during the corrosion as an internal drive, leading to elastic mismatch in the interface of oxide–metal binary medium, which is distinguishable from typical research in mechanics involving an external event (i.e. loads/displacements). In this regard, forming equilibrium between the larger oxide and smaller metal compartments, the non-linear evolution in the total swelling is properly formulated in closed-form versus the progress scale of the corrosion. The generated strains and the following stresses have been obtained for two cases of thin oxide films (i.e. 1D) and thick oxide layers (i.e. 2D), which involve both elastic deformation (i.e. reversible) and plastic corrosion (i.e. irreversible) events. The verification has been performed by tracking the formed radius of curvature from both perspectives of modelling and finite elements simulations. Furthermore, the dominant parameters for the formation of the metallic strain as well as the total swelling have been addressed. Consequently, the sensitivity of the interfacial mismatch stresses has been analytically explored versus the ratio of the elastic moduli and molar volumes. The developed swelling-induced mismatch paradigm could be used either as an indicator for the criticality of the corrosion extent, the corrosion-initiated mechanical actuation, or the material selection process for design in corrosion-prone environments, based on the volume-sensitive and mechanical properties.

1. Introduction

Oxidation of metals is a crucial factor for the safety assessment and engineering of industrial components (Young, 2008) and their operation (Knittel and Bronson, 1984), which occurs regardless of the resistance of the material under extreme conditions (Hillner, 1977). For instance, the use of corrosion-resistant zirconium Zr as a clad in nuclear reactors still sets limitations on the reactor's fuel energy extraction rate in high temperatures (Zaimovskii, 1978) and humidity (El-Sherik, 2017) which could lead to degradation (Causey et al., 2005) and possibly fracture (El Maaddawy and Soudki, 2007). The mechanisms of corrosion have extensively been investigated (Marcus, 2011), which is still ongoing using new techniques such as additive manufacturing (Sander et al., 2018).

Corrosion has mainly been investigated through the (electro)chemical/material perspective for understanding the underlying mechanism (Preuss, 2021), kinetics (Forsberg et al., 1995), passivation (Stafiej et al., 2013), irradiation (Was et al., 2011), the role of nanostructure (Mahesh and Raman, 2014) and temperature range (Yin et al., 2009) and chemical reactions (DiMeglio and Bartlett, 2017), oxide phase transformation (Chen et al., 2022), environmental sulfide (Kimura et al., 1989), fluorine (Gwinner et al., 2022) and iodine additives (Li et al., 2022), synthesizing composites (Chen et al., 2019), graphene coating to enhance thermal stability (Sun et al., 2022) and chemical composition (Kozlovskiy and Zdorovets, 2019). It has been particularly explored in the magnesium alloys (Atrens et al., 2020), biometallic materials (Singh and Dahotre, 2007), implants (Eliaz, 2019), carbon steels (Dwivedi et al., 2017), and concretes containing steel

---

* Corresponding author at: Boğaziçi University, Bebek, Istanbul, 34342, Turkey.
E-mail address: aryanfar@caltech.edu (A. Aryanfar).

[1] Contributed mainly prior to this affiliation.

[2] a.k.a. Bosphorus University.

https://doi.org/10.1016/j.ijsolstr.2025.113535
Received 7 March 2025; Received in revised form 2 June 2025; Accepted 18 June 2025

Nomenclature

Symbol	**Description**
R_{PB}	Pilling-Bedworth ratio
$\hat{R}$	1D swelling ratio.
C	Concentration of oxygen (mol m^{-3})
C_0	Ambient oxygen conc. (mol m^{-3})
t	time (s)
$s(\hat{s})$	oxide (normalized) scale (m)
D	Oxygen diffusivity /oxide (m^2 s^{-1})
k	Corrosion reaction rate (s^{-1})
h_0, l_0	bare height/width of metal (m)
G_{Ad}	adherent shear modulus (GPa)
h_{Ad}	adherent thickness (m)
P	external shear load (N)
l_T, l_{EQ}, l_B	top, equilibrium, bottom scale (m)
$\nu(\nu_O)$	Poisson ratio (Oxide)
G_M, G_O	metal/oxide shear modulus (Pa)
$\epsilon_{EQ,O}$	horizontal oxide strain at interface
σ_{xx}	horizontal stress (Pa)
A	Metal cross-sectional area (m^2)
δ	central vertical displacement (m)
r_{EQ}	Interfacial radius of curvature (m)
$V_{m,O}, V_{m,M}$	Oxide/metal molar vol. (m^3 mol^{-1})
$\delta x, \delta y$	horizontal/vertical swelling (m)
h_M	metal scale (m)
dy_M	removed metal increment (m)
dy_P, dy_E	plastic/elastic swelling (m)
E ($\hat{E}$)	elastic modulus (ratio) (Pa)
$E_O(E_1)$, $E_M(E_2)$	oxide/metal elastic modulus (GPa)
ϵ_O, ϵ_M	oxide/metal strain
$\hat{\sigma}_M$	normalized metal stress
$\sigma_{y,M}, \epsilon_{y,M}$	metal yield stress/strain
Δ ($\hat{\Delta}$)	total (normalized) swelling (m)
dx_R	infinitesimal retention (m)
τ_{UN}	uniform shear stress (Pa)
t_1, t_2	oxide/metal scales (m)
dx, dy	top corner displacements (m)
$\epsilon_{EQ,M}$	horizontal metal strain at interface
e	neutral axis distance (m)
b	depth of metal (m)
c	maximum distance from centroid (m)
$\delta\theta$	total angle span (*rad*) after bending

bars (Broomfield, 2023). Corrosion has been measured for the degradation of non-metallic elements such as plastics (Choi et al., 2007), concrete (Gaidis, 2004), and fuel cells (Dong et al., 2024). The used methods include Raman imaging (Mermoux and Duriez, 2021), visual inspection (Khasanova, 2022), setting up a new device (Wilczynska et al., 2019), and cyclic cooling (Mohanty et al., 2012).

Possessing a similar mechanism, one of the main failure mechanisms in Light Water Reactor (LWR) pipes is the stress buildup and the formation of metal–oxide layers with the underlying intact metal matrix (Motta et al., 2007). The resulting swelling, which could get localized (Jacques et al., 1999), translates to added compressive stresses (Ganser et al., 2019), which could get exacerbated in the presence of external pressure (Aryanfar et al., 2022), and could lead to the formation of cracks, particularly during cyclic cooling (Mohanty et al., 2012). Such corrosion-induced stress development has been observed via specimen extension tests (SETs) (Noden et al., 1968), deflection-based measurements (Huntz et al., 2002), and catenary (Evans and Huntz, 1994) methods, temperature variation (Stout et al., 1989), as well as X-ray diffraction microscopy (XRD) (Goedjen et al., 1997) and Raman microscopy (Birnie et al., 1992). The observed repetitive jump and slow-down pattern of the corrosion rate signifies the layer-by-layer cracking, which ultimately leads to the total fracture (El Maaddawy and Soudki, 2007). In this context, the formation of residual stresses has been explored (Fettre et al., 2015), the corrosion-induced stress growth has been measured during the heating–cooling cycles (Kurpaska et al., 2018) in local and global scales (Kurpaska et al., 2016), and during creep deflection tests (Saunders et al., 1997). Furthermore, the real-time stress measurements are more accurate than their post-facto counterpart due to amplified oxygen diffusion and increased viscoplasticity (Le Saux et al., 2018).

Although corrosion is an electrochemical event, it originates from the diffusion of oxygen solute from the water into the metal matrix (Cox, 2005), which generates internal mismatching stresses (Huang et al., 2013). Equivalent studies have investigated in the context of water-absorbing polymer gels (Drozdov and Christiansen, 2016), plastic straining (Zhao et al., 2018), lithium insertion into silicon electrodes and polymer electrolytes (Zhao and Cui, 2016), chemo-mechanics for rechargeable batteries (Zhao et al., 2019).

Modeling-wise, there have been developments of several finite elements methods (FEMs) for localized corrosion (Liu and Kelly, 2019), stochastic approaches (Li et al., 2009) and analytical (Chou et al., 2014) works, with idealizing assumptions. Furthermore, the relationship between the oxidation scale and the formed stress has been established in several modeling studies based on the diffusion (Dong et al., 2013), interface curvature (Aryanfar et al., 2022), and the superposition of the free and confined interactions between the metal and oxide (Ruan et al., 2013). Moreover, the kinetics of corrosion has been described in the form of nonlinear (Ma et al., 2023), power-linear forms (Panchenko and Marshakov, 2016), diffusion-coupled current density prediction (Seddiqi et al., 2020), coupled diffusion–reaction framework (Fatima et al., 2011), the peridynamics modeling (Jafarzadeh et al., 2019) and statistical exploration of annealing temperature on the pitting corrosion (Gholami et al., 2015).

Case studies of corrosion-induced deflection and its kinetics have previously been reported (Roy and Burgess, 1970) where the corrosion kinetics have been correlated to the radius of curvature in the growing interface (Zhang et al., 2023) as well as the geometry of the corrosion medium (Chou et al., 2014). As well, the deflection has been utilized to measure the amount of the buildup stress (Li et al., 1999) and to quantify the scale of corrosion (Huntz et al., 2007). The development of the stress has been also explored using the visco-plastic behavior (Parise et al., 1998), creep behavior (Ruan et al., 2012), in the context of thin films/coatings (Abadias et al., 2018), delamination (Stoney, 1909), swelling in the bilayer gel beams (Drozdov and Christiansen, 2016), bending (Pezzulla et al., 2016) and thermo-mechanical equilibrium in bi-layers (Abawi, 2004), core–shell quantum-dots (Yang, 2023), quasi-isotropic strands (Zhang and Wu, 2023), epitaxial mismatch (Subramaniam and Ramakrishnan, 2003), and exploring residual stress in welded components (Song et al., 2022).

One of the main attributes of corrosion, which has yet to be studied in-depth, is the formation of metal to oxide and the resulting swelling. In this regard, a considerable amount of oxygen enters the metal matrix and causes volume expansion. Such swelling, which as well occurs for non-metallic compounds in the presence of humidity (Eliseev et al., 2024), is represented by the Pilling–Bedworth ratio R_{PB} for the metals (i.e. 56% for the zirconium) (Bedworth and Pilling, 1923) and causes a substantial interfacial mismatch stress development within the metal/oxide interface. The strain growth could be explained by combining the Pilling–Bedworth ratio with an array of physical measures (Clarke, 2003). Nonetheless, the Pilling–Bedworth ratio remains a strong indicator of the increase in molar volume and an initiator of mismatch stress (Xu and Gao, 2000), which has not been sufficiently explored for predicting the mechanical failure of metals. Hence the current understanding on the chemistry of the corrosion could be complemented from the viewpoint of the mechanics.

Table 1
Typical corrosion parameters for zirconium Zr.

Parameter	D	k	C_0	s
Value	1.4×10^{-20}	7.1×10^{-6}	55×10^3	1
Unit	$m^2\ s^{-1}$	s^{-1}	$mol^2\ m^{-3}$	mm
Ref.	De González and García (1990)	Zhang et al. (2007)	Calculated	Assumed

In this paper, a corrosion-state dependent one and two-dimensional frameworks have been developed for the evolution of the elastic mismatch strains/stresses versus the corrosion progress, with a simplified environment as the boundary. In this regard, the initial stages of corrosion is focused on, since the other age-related effects leading to degradation/disintegration, such as (electro) chemical factors have not dominated the corrosion yet, and the mechanical interactions are still in the elastic regime of behavior. Starting from an infinitesimal swelling due to volume augmentation during the transition of metal to oxide, and considering the difference in their respective mechanical properties, we have defined dimensionless parameters and established a constitutive paradigm for obtaining the interfacial equilibrium scale between oxide and metal. Subsequently, we have quantified the total amount of swelling and the internal strains/stresses, as well as the resulting curvature for the candidate materials. The paradigm is verified with the finite element simulations and the correlation of the mismatch strain with the physical properties has been explored further. The obtained physics could be useful for understanding the mechanics of the corrosion and the attributed deformation as well as the material-selection process during the design for the corrosion-sensitive environments.

2. Methodology

The gradual corrosion in the thin films and metal layers causes swelling in the surface, due to infiltration of oxygen and formation of oxide, considering that the oxide compound takes more volume than the corresponding metal. Such volume augmentation is characterized by the Pilling–Bedworth ratio R_{PB} (Bedworth and Pilling, 1923) as:

$$R_{PB} = \frac{V_{m,O}}{V_{m,M}} \tag{1}$$

where $V_{m,O}$ and $V_{m,M}$ are molar volumes of oxide and metal for the given specific material.

Barring a few exceptions, the volume of the oxide is larger than the equivalent metal distinguishably ($R_{PB} > 1$). Considering the metal yielding strain in the order of $\sim 10^{-3}$, the developed mismatch strains can easily cause failure and lead to plastic deformation, which is central to the developed mismatch framework.

2.1. Kinetics

Since the chemical aspects of corrosion such as passivation, formation of side-products (i.e. hydroxides), phase transformation, etc., have been thoroughly investigated in the past, herein we focus on the mechanical aspect of corrosion. During a typical corrosion event, the oxide layer forms through the simultaneous diffusion of oxygen, deep down into metal matrix, as well as the diffusion of metal, up to the surface of the medium (Young, 2008; Birks et al., 2006). While the former event causes local expansion in depth and forms mismatch in larger scale, particularly between the deformed oxide and undeformed metal, the latter mechanism forms more of stress-free oxide on the exposed surface, which grows similar to the electrodeposition event. In this study, we have conservatively considered only oxygen diffusion as extreme case scenario, leading to the build-up of the maximum possible stress in the limit. In such case, the infiltrated oxygen meets the corrosion interface in depth. The oxygen transition in depth of y from the surface can be expressed as the trade-off between diffusive influx/out-flux of the ions ($DIFF$) as well as their consumption via reaction (RXN), summarized as follows Reyes et al. (2018):

$$\frac{\partial C}{\partial t} = \left(\frac{\partial C}{\partial t}\right)_{DIFF} - \left(\frac{\partial C}{\partial t}\right)_{RXN} \tag{2}$$

In order to compare the rates of diffusion $DIFF$ and reaction RXN, the typical values for the corrosion of zirconium are used as given in Table 1[3].

Hence, one can compare the order of the diffusion term in the oxide scale s versus the reaction term, as:

$$\begin{cases} \left(\frac{dC}{dt}\right)_{\text{Diff}} \sim D\frac{C_0}{s^2} \sim 10^{-22}\ \text{mol s}^{-1} \\ \left(\frac{dC}{dt}\right)_{\text{Rxn}} \sim kC_0 \sim 10^{-1}\ \text{mol s}^{-1} \end{cases} \tag{3}$$

which yields:

$$\left(\frac{\partial C}{\partial t}\right)_{RXN} \gg \left(\frac{\partial C}{\partial t}\right)_{DIFF} \tag{4}$$

The interpretation of the reaction rate being far more dominant than that of diffusion, with a significant gap, is that the oxygen is consumed immediately upon reaching the reaction sites and the diffusion into the inner depth of corrosion is only possible when the corrosion interface is saturated to the full stoichiometric limit. In other words, during the further progress of the oxide layer, no tangible variation in the concentration profile in depth should be observed, since the previous oxide layers are stoichiometrically saturated by reaction, and observe no consumption. As well, since the growth rate in the interface of metal/oxide is considerably slow, it could be treated in quasi steady-state form.

2.2. Corrosion characterization

The oxide layer typically is a heterogeneous medium containing grains, where the oxide expansion can occur through their boundaries (Rhines and Wolf, 1970). For simplicity in this work we assume this medium to be homogeneous. While the diffusion in atomic scale could be attributed to oxygen flow into the metal matrix (Pemsler, 1958), in the larger scales could occur through the diffusion of oxygen into the grain boundaries of the grown columnar oxide grains (Rhines and Wolf, 1970). Regarding the side-corrosion, in the very initial stage of corrosion, the formed oxide layer has extreme aspect ratio (thin height and long width). Hence, the horizontal real-estate is the entire surface (top) and the vertical real-estate (left/right) is very thin. Therefore the contribution of side-corrosion will be insignificant. As well, certain domains lack side-exposed boundaries, such as pipes with the rounded geometry makes the left and right boundaries eventually connected together. Therefore a significant portion of the corrosion continues to occur though the top surface.

In order to understand/calculate the internal mismatch stresses and deformation between the formed oxide (i.e. surface) and the metal (i.e. inner bulk), we perform superposition and decompose the oxidation into two steps. Hence initially the oxide grows freely and later on it gets confined by the underneath metal layer.

---

[3] The molar concentration of the water can simply be calculated as:

$$C_0 = \frac{\rho}{M} = \frac{1000gr\ L^{-1}}{18gr\ mol^{-1}} = 55\ \text{mol L}^{-1}$$

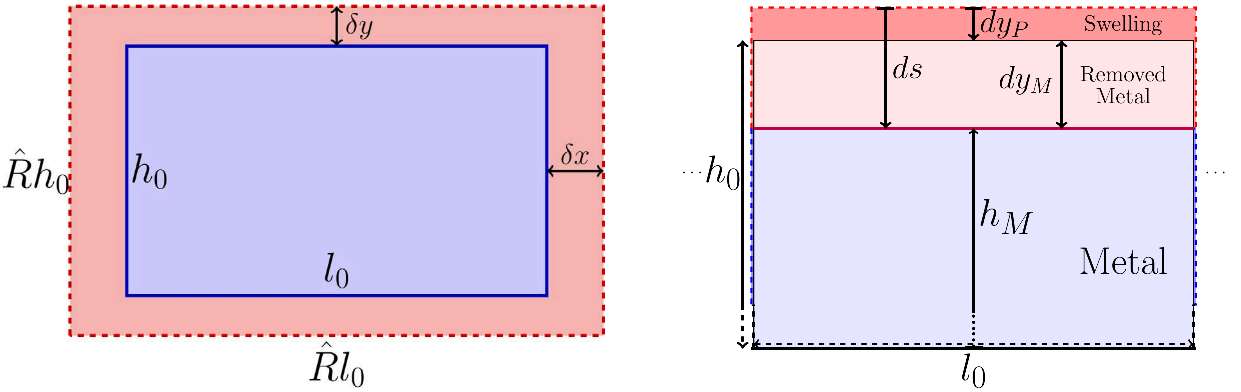

(a) Isotropic expansion of metal to oxide during the free expansion. The volume ratio is R_{PB} leads to the one dimensional expansion of $\hat{R} = \sqrt[3]{R_{PB}}$ in each 3 directions.

(b) The volumetric characterization of the swelling from corrosion where the infinitesimal removal of metal thickness dy_M (smaller), is replaced by its transformed oxide thickness ds (larger). Hence their difference leads to infinitesimal plastic swelling dy_P. $h_0 \times l_0$: original metal height and length, h_M: instantaneous metal height.

Fig. 1. (a) Free transformation and swelling of a metal piece into oxide. (b) The characterization of infinitesimal plastic swelling dy_P versus the infinitesimal corrosion ds.

As illustrated in Fig. 1(a), the original metal of dimensions $l_0 \times h_0$, can isotropically expand in all directions and end up in a new oxide form, which is characterized by the volume expansion given in Equation (1). Hence during the 3-dimensional free expansion, each side grows with the scale of $\hat{R} = \sqrt[3]{R_{PB}}$.

The corrosion in this work is tracked versus the progress in the thickness of oxide scale s, which gradually grows from the surface of the metal in quasi steady-state form, until ideally spanning to the entire medium (i.e. $0 < s < \hat{R}h_0$). Fig. 1(b) illustrates that an infinitesimal metal scale dy_M is replaced by a slightly larger new infinitesimal oxide scale ds, where $ds = \hat{R}dy_M$. In such trade-off, the infinitesimal plastic swelling dy_P can be calculated from the difference of formed oxide versus the vanished metal as (Aryanfar et al., 2022):

$$dy_P \approx \frac{\hat{R}-1}{\hat{R}} ds \tag{5}$$

therefore, for the initial metal height of h_0, the instantaneous total height due to corrosion scale s would be $h_0 + \frac{\hat{R}-1}{\hat{R}} s$, which is composed of both metal and oxide, and the remaining metal scale $h_M(s)$ would be:

$$h_M(s) = h_0 - \frac{s}{\hat{R}} \tag{6}$$

2.3. 1D modeling (thin films)

Fig. 2(a) shows an experimental sample of an oxide layer formed on top of a metal substrate (Lin et al., 2017). Having different volumes and a common interface scale, a mismatch stress develops in both layers. This can be explained more clearly via the superposition into initial free expansion of a metal piece (l_0) into oxide ($\hat{R}l_0$) and its later confined retention to reach static equilibrium (l_{EQ}) as illustrated in Fig. 2(b). Hence the mismatch stresses develop within either media internally. Such stress for the oxide is compressive (→←) due to resistance to free expansion, and vice versa tensile stress (←→) is generated within the metal due to imposing enlargement via the upper oxide in their interface.

For 1D approximation (i.e. thin film), considering the plane stress condition, the stress variation in the vertical direction could be considered as negligible, forming a rectangular stress profile. Hence, the static equilibrium ($\sum F_x = 0$) yields:

$$E_O \epsilon_O s \approx E_M \epsilon_M \left(h_0 - \frac{s}{\hat{R}}\right) \tag{7}$$

where the approximation sign is due to assumption of uniform stress distribution in the vertical direction. Having the individual strains as $\epsilon_O = \frac{\hat{R}l_0 - l_{EQ}}{\hat{R}l_0} < 0$, $\epsilon_M = \frac{l_{EQ} - l_0}{l_0} > 0$, one gets the final equilibrium scale l_{EQ} as:

$$l_{EQ} \approx \frac{\hat{R} + \left(\hat{R}\hat{E} - 1\right)\hat{s}}{\hat{R} + \left(\hat{E} - 1\right)\hat{s}} l_0 \tag{8}$$

where $\hat{E} = \frac{E_O}{E_M}$, and $\hat{s} = \frac{s}{h_0}$ are the ratio of elastic moduli and the relative progress of the corrosion respectively.

2.3.1. Metal stress

Having the equilibrium scale l_{EQ} as an intermediate between the smaller and larger medium $\left(l_0 \le l_{EQ} \le \hat{R}l_0\right)$, one can obtain the metallic strain as $\epsilon_M = \frac{l_{EQ} - l_0}{l_0} > 0$. For small corrosion amount, the material behaves in the elastic (i.e. linear) regime. Hence the formed metallic stress σ_M would be obtained which can get normalized as:

$$\hat{\sigma}_M \approx \frac{1}{\epsilon_{y,M}} \frac{\hat{E}\left(\hat{R} - 1\right)\hat{s}}{\hat{R} + \left(\hat{E} - 1\right)\hat{s}} \tag{9}$$

where $\hat{\sigma}_M = \frac{\sigma_M}{\sigma_{y,M}}$ is the normalized metallic stress, $\sigma_{y,M}$ and $\epsilon_{y,M}$ are the metal yield stress and strain respectively.

2.3.2. Total swelling Δ

The total swelling Δ is the cumulative result of the infinitesimal corrosion-induced (i.e. plastic) swelling dy_P - due to stoichiometric reaction with the oxygen- as well as the elastic swelling dy_E - due to lateral confinement from the underneath metal (i.e. Poisson's effect), as:

$$d\Delta = dy_P + dy_E \tag{10}$$

While the plastic swelling was previously obtained in Eq. (5), the elastic swelling can get calculated via the superposition steps as shown in Fig. 3. Since the top (and bottom) surfaces are traction-free $\sigma = 0$, they will experience a higher amount of swelling resulted from the corrosion. Conversely, the lateral directions will experience lower amounts of swelling and will have partial deformation. Therefore, the elastic swelling can be broken down to the initial free expansion of the original

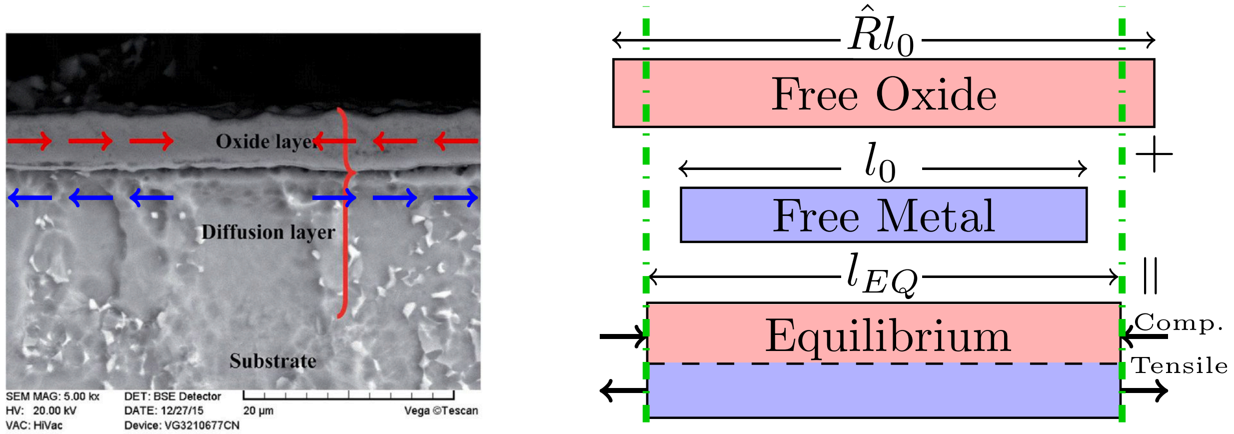

(a) SEM visualization of the grown oxide layer, illustrating the compressive stress in oxide (red) and tensile stress in metal (blue). Modified and reprinted with permission from ref. [92] Copyright 2019 Royal Society of Chemistry.

(b) The mechanical equilibrium between the freely expanded oxide with the scale of $\hat{R}l_0$ (top) and the underneath intact metal of the original scale l_0 (middle), leading to the common equilibrium scale of l_{EQ} (bottom, highlighted in dashed green). The respective compressive/tensile stresses in equilibrium are illustrated.

Fig. 2. (a) Experimental image of metal/oxide cross-section. (b) Static equilibrium between the transformed oxide (larger) and remaining metal (smaller).

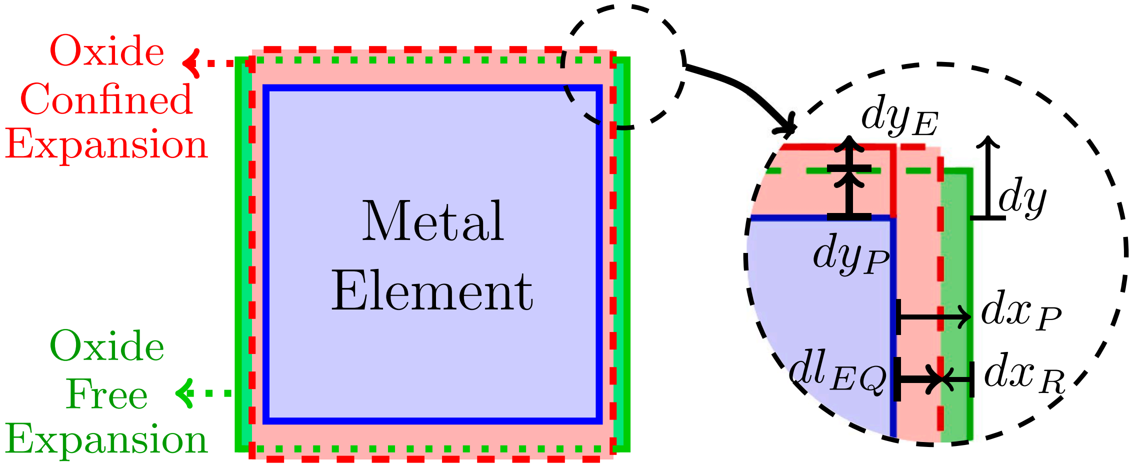

Fig. 3. The swelling during the transition of the infinitesimal metal element (blue) to oxide could be simplified by the superposition to an initial free expansion (green) on the corroded portion followed by a confined horizontal retention (red) to reach the static equilibrium with the underneath metal (not shown here). In the first step, the oxide free expansion (i.e. swelling) generates the plastic (i.e. irreversible) displacements of dx_P (horizontal) and dy_P (vertical) whereas later on, the confined side-retention of dx_R leads to extra elastic vertical expansion dy_E due to Poisson's effect. ($R_{PB} > 1$).

metallic medium (blue to green) and later confined retention (green to red). In the second step, the Poisson effect describes the relationship between the vertical ϵ_y and horizontal ϵ_x strains by magnitude as:

$$\frac{dy_E}{s} = \nu_O \frac{dx_R}{\hat{R}l_0} \tag{11}$$

and the magnitude of infinitesimal retention dx_R is obtained as:

$$\begin{aligned} dx_R &= \hat{R}l_0 - l_{EQ} \\ &= \frac{\left(\hat{R}-1\right)\left(\hat{R}-\hat{s}\right)}{\hat{R}+\left(\hat{E}-1\right)\hat{s}} l_0 \end{aligned} \tag{12}$$

We note that, such correlation between the retention dx_R and the corrosion scale $\hat{s}$ is independent of larger scale geometry (thin, or thick) and occurs for the infinitesimal element of the material.

Finally the total normalized swelling $\hat{\Delta}$ is obtained via replacement of Eqs. (12), (11), and (5) into the relationship (10) as:

$$\hat{\Delta} = \frac{\hat{R}-1}{\hat{R}} \left(1 + \nu_O \frac{\left(\hat{R}-\hat{s}\right)}{\hat{R}+\left(\hat{E}-1\right)\hat{s}}\right) \hat{s} \tag{13}$$

where $\hat{\Delta} = \frac{\Delta}{h_0}$ is the normalized total swelling of the metal/oxide composite medium.

2.4. 2D modeling (thick layers)

Fig. 4(a) illustrates the geometry of the connection between the oxide (i.e. larger, top) and metal (i.e. smaller, bottom) layers with the resulting curvature due to expansion via infiltration of oxygen O_2. Due to symmetry, the left/right distributions will be identical, hence one narrow-down to the half scale. Herein we elaborate on the mechanical equilibrium, both in the interface and within each component, as below:

2.4.1. Shear stresses

Fig. 4(b) illustrates the free body diagram for both metal (lower) and oxide (upper) layers, separated in their interface. In order to obtain the distribution of the shear stress, one can notice that due to symmetry in the central cross-section, the shear stress should be both in opposite

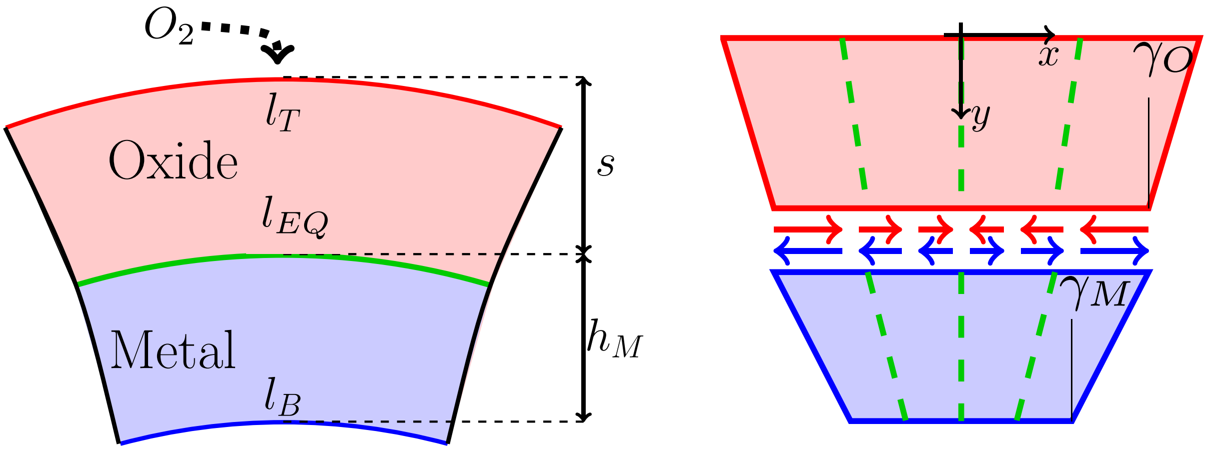

(a) The formed geometry scheme as the outcome of interaction of oxide (top, larger) and metal (bottom , smaller), which go under compression and tension respectively and lead to the top l_T , equilibrium (i.e. interfacial) l_{EQ} and bottom l_B scales respectively in the mechanical equilibrium. The instantaneous oxide s and metal h_M scales are illustrated.

(b) Projected shear stress distribution in the oxide/metal interface which undergo compression and tension respectively. Due to symmetry, the shear strain γ in the central zone vanishes, while it grows when moving horizontally towards the left/right boundary. The dashed lines approximate the final deformed pattern of the vertical infinitesimal elements.

Fig. 4. The characterization of the (a) deformed shape and (b) interfacial stresses during the corrosion of a thick (i.e. 2D) metallic layer.

directions (action–reaction) and be equal (symmetry) simultaneously, hence it will vanish ($\tau = 0$). In other words, due to expansion to the sides, the shear stress in the left half should be to the left direction and vice versa in the right half, to the right. Hence in the center is should yield to zero in the middle. This has been illustrated as the vertical dashed green line in the center ($x = 0$), which remains undeformed. However, moving towards the left/right boundaries ($x \to \pm \frac{l_{EQ}}{2}$) along the oxide–metal interface, the original vertical planes will get distorted and become more and more tilted since the boundaries are traction-free and more relax than the center. Hence, since the shear stress correlated with the slope of the deformed planes ($\tau \propto \gamma \sim \frac{dx}{dy}$) one needs to adopt a distribution for the shear stress between two layers, which starts from zero ($\tau = 0$) in the center, and increases monotonously towards the boundaries in a certain form. We interpret the metal–oxide interaction as two distinct layer with the possibility of sliding/resisting against each other to a certain extent.

Several models have developed the distribution of shear stress along the interface of the two components, which tend to drop from the external location . In this regard, typically the shear lag model has been used between two distinct layers (Dillard, 2002), in the surface-attached optical fiber sensors (Duck et al., 1999), and for estimating the crack density in laminates (Singh, 2018). The shear distribution in the shear lag model, which additionally contains the inter-layer adherent component, highly depends on the mechanical response (i.e. flexibility) of the adherent (Mojdehi et al., 2017). In the extreme cases, two distinct shear stress profiles have been proposed for the highly stiff (i.e. rigid) versus the highly loose (i.e. flexible) mechanical behavior of the adherent (Dillard, 2002). Any type mechanical behavior in a bonding between two layers is expected to fall in between these two extreme states, including the chemical bonding in the interface of oxide and metal layers. The distribution of the shear stress in these two extreme conditions provides the upper/lower bounds for the shear stress distribution and can help to obtain an interpolated shear stress profile. In particular the visualization can helpful for interpolation. As a case-study, we consider a medium of 1 cm × 1 cm and assume 5% progress in the scale of corrosion (i.e. $\hat{s} = \frac{1}{20}\hat{R}$ and $\hat{R}$ being the entire extent of the corrosion). Therefore, the remaining metal scale would be $h_M = 0.95\hat{R}h_0$ and the progressing oxide scale h_O would have the value of $h_O = \frac{h_0}{20}\hat{R}$. Table 2 illustrates a sample geometry, and the Table 3 (later) provides the material properties for the sample metal (i.e. Zr). Due to the absence of adherent, the interfacial shear modulus A_{Ad} is assumed to be the average of the oxide and metal and the interfacial adherent thickness h_{Ad} is assumed very small compared to the oxide and metal scales.

Table 2
Parameters for calculating shear stress. The selected is zirconium Zr .

Parameter	h_0	l_0	s	h_M	P	G_{Ad}	h_{Ad}
Value	2	2	1.16	1	100	56.5	1
Unit			cm		N	GPa	mm

In the case of rigid adherents, the uniform shear stress τ_{UN} is formed, per unit of depth ($1m$), which can simply calculated as:

$$\tau_{UN} = \frac{P}{l} = \frac{100}{2 \times 10^{-2}} = 5 \times 10^3 \mathrm{N/m} \tag{14}$$

and for the case of flexible adherent the shear stress τ_{FL} is obtained from the static equilibrium has (Dillard, 2002):

$$\tau_{FL}(x) = \frac{P\omega}{2\sinh\left(\frac{\omega l}{2}\right)}\cosh(\omega x) + \frac{P\omega}{2\cosh\left(\frac{\omega l}{2}\right)}\frac{E_2t_2 - E_1t_1}{E_1t_1 + E_2t_2}\sinh(\omega x) \tag{15}$$

where x is the horizontal distance from the central axis, P is the applied shear force, and E_1, E_2 and t_1, t_2 are the elastic moduli and thickness of the media 1 and 2 respectively. Meanwhile, ω is the coefficient expressed as :

$$\omega = \sqrt{\frac{G_{Ad}}{h_{Ad}}\left(\frac{E_1t_1 + E_2t_2}{E_1t_1E_2t_2}\right)} \tag{16}$$

Therefore, the shear stress grows exponentially from the center and reaches the maximum value at the far end (i.e. $x = \frac{l}{2}$).

Replacing the geometrical and material properties of the oxide (with the index $\square_1$) and metal (the index $\square_2$) in Equations (15) and (16), from Tables 2 and 3 (next section), and including Eq. (14), one gets the two shear stress profile visualized in Fig. 5(a), which differ due to mechanical behavior of the adherent (rigid ↔ flexible). Hence for the corrosion event, where the oxide/metal interface is chemically-bonded and is not externally loaded, the projected shear stress profile

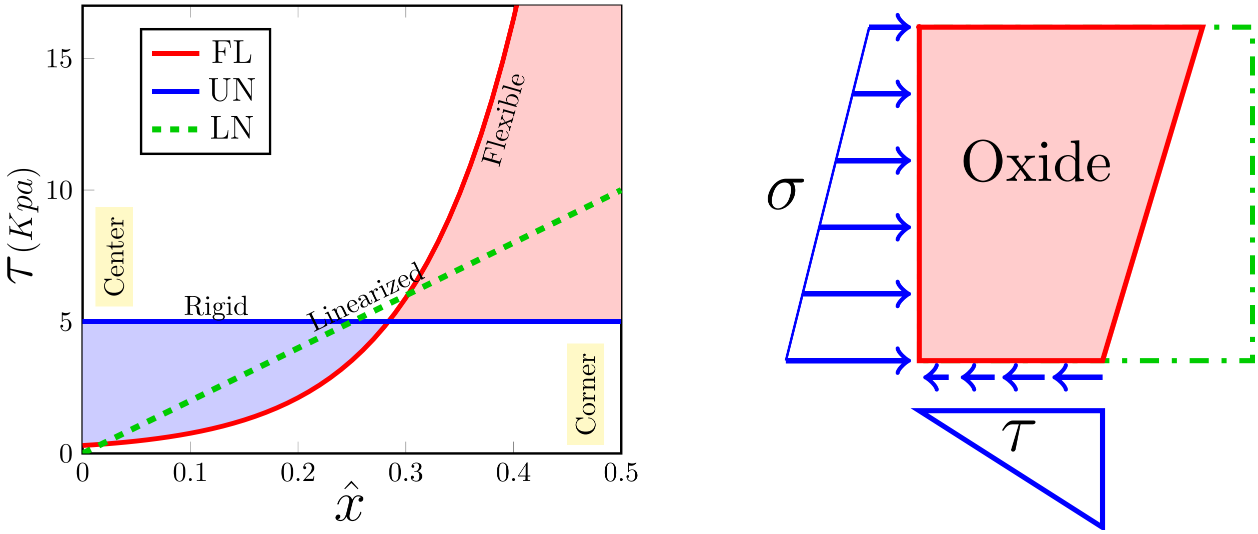

(a) The profile of the shear stress between two layers in the presence extreme cases of flexible adherent (red), rigid adherent (blue), which, when averaged, leads to the adopted linearized distribution (dashed green).

(b) The linearization of the stress distributions, leading to equilibrium between half-oxide shear and compressive stresses. The compressive stress is at its maximum in the interface and relaxes, moving further away from it, which is approximated via trapezoidal distribution.

Fig. 5. Estimation of the (a) shear stresses profile between oxide and metal and (b) the static equilibrium between the compressive and shear stresses in half-oxide.

is assumed to be the average of the two aforementioned extreme profiles, with a linear variation versus the distance (i.e. dashed green line). Needless to mention that although the shown profiles in Fig. 5(a) are obtained for specific scale of corrosion ($\hat{s} = 0.05\hat{R}$), same correlation is obtained for any other extent of the corrosion $\hat{s}$, as well as any considered force P, where the linearized case (Fig. 4(b)) falls in between the two extreme cases of rigid and flexible adherents.

In the interface of the oxide and metal, the slopes are correlated with the shear modulus ($\tau = G\gamma$) via *action–reaction* mechanism, where the harder the medium ($G \uparrow$), the less it twists ($\gamma \downarrow$). Hence, setting $\tau_M = \tau_O$ in the extreme outer boundary, and considering the plain stress condition, one gets the following:

$$G_O \frac{l_T - l_{EQ}}{s} \approx G_M \frac{l_{EQ} - l_B}{h_0 - \frac{s}{\hat{R}}} \tag{17}$$

where simplification leads to:

$$\left(\hat{G}\hat{h}\right) l_T - \left(1 + \hat{G}\hat{h}\right) l_{EQ} + l_B \approx 0 \tag{18}$$

where $\hat{G} = \dfrac{G_O}{G_M}$ is the ratio of the shear modulus between oxide and metal media.

2.4.2. Normal stresses

For the $2D$ corrosion development shown in Fig. 4(a), the stress is the highest in the interface of the oxide and metal, while moving vertically away from the interface the compression/tension stresses are relaxed. Assuming that the layers are thin enough such variation could get linearized, which forms a trapezoidal stress distribution during the elastic behavior, which is illustrated in Fig. 5(b).

Therefore a horizontal statics equilibrium ($\sum F_x = 0$) is established between the formed oxide (i.e. $[0, s]$) and metal (i.e. $\left[s, h_0 + \frac{\hat{R}-1}{\hat{R}} s\right]$) in the central cross-section. Considering the magnitudes of the forces in the compressive (oxide) and tensile (metal) zones, one has:

$$\int_0^s E_O \left(\epsilon_T + \epsilon_{EQ,O}\right) dy \approx \int_s^{h_0 + \frac{\hat{R}-1}{\hat{R}} s} E_M \left(\epsilon_B + \epsilon_{EQ,M}\right) dy$$

where $\epsilon_T = \dfrac{\hat{R}l_0 - l_T}{\hat{R}l_0}$, $\epsilon_{EQ,O} = \dfrac{\hat{R}l_0 - l_{EQ}}{\hat{R}l_0}$, $\epsilon_{EQ,M} = \dfrac{l_{EQ} - l_0}{l_0}$ and $\epsilon_B = \dfrac{l_B - l_0}{l_0}$. Hence, replacing into Equation above and simplifying, one gets:

$$\hat{E}l_T + \left(\hat{E} + \hat{h}\hat{R}\right) l_{EQ} + \hat{h}\hat{R}l_B \approx 2l\hat{R}\left(\hat{E} + \hat{h}\right) \tag{19}$$

where l_T, l_{EQ} and l_B are the top, interfacial and bottom scales, respectively as shown in Fig. 4(a) ($l_B < l_{EQ} < l_T$) and $\hat{h}$ is the relative scale of the metal to oxide $\hat{h} := \dfrac{h_M}{h_O} = \dfrac{1}{s}\left(h_0 - \dfrac{s}{\hat{R}}\right)$.

2.4.3. Oxide equilibrium

The oxide compartment during the corrosion contains equilibrium per se, which is attained from the balance between the normal σ and shear τ stresses in the top quadrant. As shown in the free body diagram of Fig. 5(b), the equilibrium between the forces due to normal σ and shear τ stresses yields:

$$\frac{1}{2}\tau_{max}\frac{l_{EQ}}{2} \approx \frac{E_O}{2}\left(\epsilon_T + \epsilon_{EQ,O}\right) s \tag{20}$$

where $\tau_{max} = G_O \dfrac{l_T - l_{EQ}}{2s}$ is the maximum shear stress in the interface, occurring in the boundary. Therefore replacing for the maximum shear stress τ_{max} and strains $\epsilon_T, \epsilon_{I,O}$ in terms of the scales l_T, l_{EQ} and l_B, and performing further simplification one gets the following quadratic relationship as:

$$\left(\frac{G_O}{4s}\right) l_{EQ}^2 - \left(\frac{G_O l_T}{4s} + \frac{E_O s}{\hat{R}l_0}\right) l_{EQ} + \frac{E_O s}{\hat{R}l_0}\left(2\hat{R}l_0 - l_T\right) = 0 \tag{21}$$

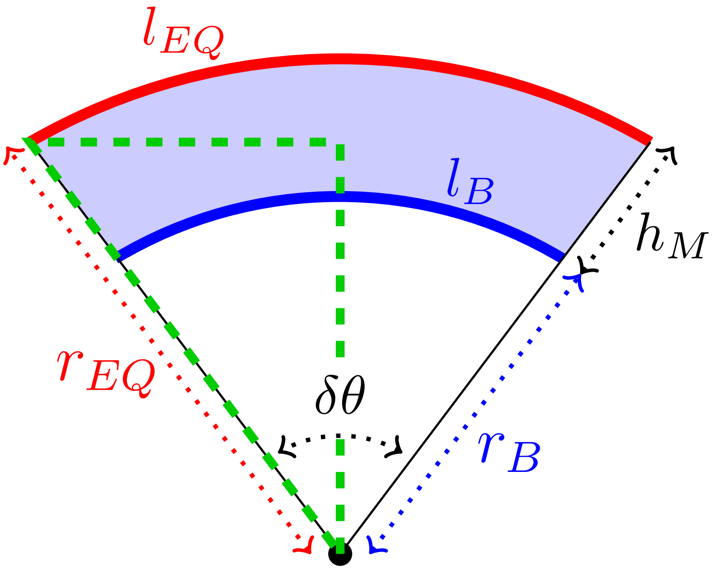

Fig. 6. The deformation in the metal compartment with the remaining scale h_M, illustrating the bottom and interfacial corrosion scales l_B, l_{EQ} with their respective radius of curvature r_B, r_{EQ}. In the model, the concentric relationships between the bottom and interface obtains the interfacial radius of curvature r_{EQ}, whereas in the simulations, the Pythagorean theorem (i.e. dashed triangle) is used for this purpose.

Eq. (18), (19), and (21) are 3 non-linear relationships, with the three unknown scales l_T, l_{EQ}, and l_B. Performing extensive algebraic grouping and simplifications leads to the following quadratic relationship for attaining the equilibrium scale l_{EQ} :

$$\boxed{A_2 l_{EQ}^2 + A_1 l_{EQ} + A_0 = 0} \tag{22}$$

where the coefficients A_2, A_1 and A_0 are extracted as:

$$\begin{cases} A_2 = \dfrac{G_O}{2}\left(\hat{E} + \hat{h}\hat{R}\right) \\ A_1 = \dfrac{2E_O s^2}{l_0}\left(1 + \hat{h}\hat{G}\right)\hat{h} - \dfrac{G_O \hat{R} l_0}{2}\left(\hat{h} + \hat{E}\right) \\ A_0 = -2E_O s^2\left(1 + \hat{h}\hat{G}\hat{R}\right)\hat{h} \end{cases} \tag{23}$$

Replacing the obtained equilibrium scale l_{EQ} into Eq. (21), one gets the top scale l_T as:

$$l_T = B_0 l_0 + B_1 l_{EQ}$$

where:

$$B_0 = \frac{2\hat{E}\left(\hat{h} + \hat{E}\right)}{\hat{E} - \hat{h}^2\hat{G}\hat{R}} \quad , \quad B_1 = \frac{\hat{h}^2\hat{G}\hat{R} + 2\hat{h}\hat{R} + \hat{E}}{\hat{h}^2\hat{G}\hat{R} - \hat{E}}$$

Finally, the bottom scale l_B is achieved via replacing the top l_T and equilibrium l_{EQ} scales into Equation (18), as:

$$l_B = C_0 l_0 + C_1 l_{EQ} + C_2 l_T$$

where:

$$C_0 = 2\left(1 + \frac{\hat{E}}{\hat{h}}\right) \quad , \quad C_1 = -1 - \frac{\hat{E}}{\hat{h}\hat{R}} \quad , \quad C_2 = -\frac{\hat{E}}{\hat{h}\hat{R}}$$

Having the top l_T, interfacial equilibrium l_{EQ} and bottom l_B scales, one could additionally calculate the formed radius of curvature in either medium. Hence, isolating the metal layer, with the scale $h_0 - \frac{s}{\hat{R}}$ (i.e. Eq. (6)) as shown in Fig. 6, one could write the radial relationships for its top (l_{EQ}) and bottom (l_B) scales. Assuming the center of curvature in the bottom and interfacial layers are nearly identical, one could write the radial correlation as:

$$\begin{cases} l_{EQ} = \left(r_B + h_0 - \dfrac{s}{\hat{R}}\right)\delta\theta \\ l_B = r_B\delta\theta \end{cases}$$

where $\delta\theta$ is the infinitesimal angle covering the aforementioned scales, r_B is the radius of the curvature in the bottom of the metal. Dividing and simplification leads to the bottom radius of curvature r_B as:

$$r_B = \frac{l_B}{l_{EQ} - l_B}\left(h_0 - \frac{s}{\hat{R}}\right)$$

From Fig. 6, one can notice that $r_{EQ} = r_B + h_M$, which after simplification finally yields:

$$r_{EQ} \approx \frac{l_{EQ}}{l_{EQ} - l_B}\left(h_0 - \frac{s}{\hat{R}}\right) \tag{24}$$

Here the approximation sign is used since the identical curvature center of bending is assumed for both the interfacial (i.e. l_{EQ}) and bottom (i.e. l_B) boundaries.

3. Simulations

The simulations were carried out, using the ABAQUS finite element software, where the metallic layer was isolated from the oxide layer the external effect from the oxide layer was imposed manually. The compartments of the simulations are described below:

For the geometry, a 2D beam was created with the dimensions of 10 cm × 1 cm and the properties of the candidate materials, were assigned from the Table 3. During the corrosion, the reduced instantaneous metal scale versus the progress of the corrosion (i.e. $\hat{s}$) was calculated from Equation (6), which is due to conversion to oxide.

Since the source of mismatching is internal, and there are no external forces, there would have been no need for placing the external reactions. However due to the requirement of the ABAQUS software, the placement of the external reactions is necessary. Therefore, the locus of the reactions should be chosen such not to interfere in the simulation results. In this regard, the neutral axis for bending should be chosen as their appropriate location. Such bending could be emulated as the effect of an eccentric tensile force F in the distance of e from the centroid of the cross-section, which additionally generates the moment $M = Fe$. Hence, the resulting stress σ will be the superposition of both factors as:

$$\sigma = \frac{F}{A} - \frac{Fec}{I}$$

Table 3
Physical/Mechanical parameters used for the candidate materials in the modeling and simulation ($h_0 = 0.01$ m, $l_0 = 0.1$ m).

Parameter	Zr	Ref.	Al	Ref.	Mg	Ref.
R_{PB}	1.57	Forsberg et al. (1995)	1.28	Cramer et al. (2003)	0.8	Cramer et al. (2003)
E_M (GPa)	94.5		69[b]		45	
$\sigma_{y,M}$ (MPa)	207	Callister Jr. and Rethwisch (2020)[a]	34	Callister Jr. and Rethwisch (2020)	220	Callister Jr. and Rethwisch (2020)[c]
ν	0.35		0.33		0.35	
E_O (GPa)	175	Azom[d]	314	Azom[e]	300	Azom[f]
ν_O	0.27		0.27		0.36	
G_M (GPa)	35	Eq. (27)	25.9	Eq. (27)	16.6	Eq. (27)
G_O (GPa)	78		156		83	

[a] The elastic modulus E_O for zirconium oxide is with 97% purity (3% remainder being Y_2O_3).
[b] For the alloy 1100 with 99% purity.
[c] For the alloy AZ31B with 97% purity.
[d] https://www.azom.com/properties.aspx?ArticleID=133
[e] https://www.azom.com/properties.aspx?ArticleID=52
[f] https://www.azom.com/properties.aspx?ArticleID=54

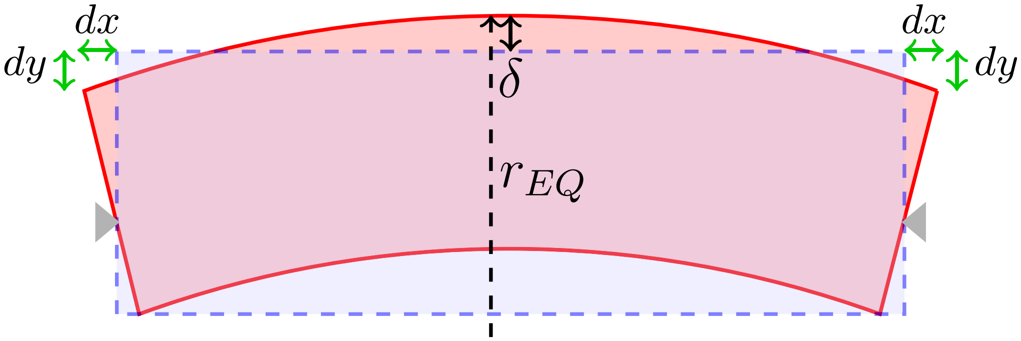

Fig. 7. Replicated simulation setup via imposing the infinitesimal horizontal (i.e. δx) and vertical (i.e. δy) displacements the corner of the metal compartment, which results in the central vertical displacement δ and the interfacial radius of curvature r_{EQ}. Background blue: undeformed geometry, foreground red: deformed metal after corrosion.

where the subtraction sign is for the lower half. The cross-sectional area of metal with the in-plane depth of b is $A = b\left(h_0 - \frac{s}{\hat{R}}\right)$ and its moment of inertia is $I = \frac{b}{12}\left(h_0 - \frac{s}{\hat{R}}\right)^3$. Therefore, the location of neutral axis e would be obtained by setting $\sigma = 0$ as (Freund and Suresh, 2004):

$$e = \frac{1}{6}\left(h_0 - \frac{s}{\hat{R}}\right) \tag{25}$$

such location of the neutral axis from the center is equivalent to the distance of $\frac{1}{3}$ of the total height (i.e. $\frac{1}{6}\left(h_0 - \frac{s}{\hat{R}}\right)$), from the bottom.

The bending of the metal, which is illustrated in Fig. 4(a) (lower blue compartment) is replicated via displacing its top corners to the prescribed horizontal dx and vertical dy values as an external boundary condition from the oxide layer. Such deformation is emulated in Fig. 7, where an equal stretching as horizontal side openings $dx(\hat{s})$ were assigned in both top ends, the magnitude of which is obtained from Equation (22). The horizontal displacement dx is obtained from the difference of equilibrium (i.e. $l_{EQ}(\hat{s})$) and the original (i.e. l_0) scales, as:

$$dx(\hat{s}) = \frac{1}{2}\left(l_{EQ}(\hat{s}) - l_0\right) \tag{26}$$

Here the equilibrium scale l_{EQ} was calculated versus the progress scale of the corrosion $\hat{s}$ the 3 candidate material properties, given in Table 3 where the shear moduli G are correlated with the elastic modulus E and Poisson ratio ν as:

$$G = \frac{E}{2(1+\nu)} \tag{27}$$

Such horizontal displacement $dx(\hat{s})$ is inevitably accompanied by a vertical displacement $dy(\hat{s})$, due to bending-induced rotation of side planes around the neutral axis (i.e. $\frac{2}{3}h_M$ from above corner) and the trigonometry leads to:

$$dy(\hat{s}) = \frac{2}{3}h_M - \sqrt{\left(\frac{2}{3}h_M\right)^2 - dx(\hat{s})^2} \tag{28}$$

In order to distinguish the locus of the imposed displacements (dx, dy) as well as the reaction (i.e. neutral axis), thin planar extrudes were created on the original domain geometry and the external displacement (resulted from the oxide) as well as the zero displacement (reaction), were applied to them. Afterwards, the meshing was performed and the simulations were run consequently.

Additionally, the resulting curvature leads to the upward vertical displacement δ, in the center, with the interfacial radius of curvature of r_{EQ}. In this regard, noting the Pythagorean theorem in the formed triangle in Fig. 6, the horizontal edge is obtained from Fig. 7 as $\frac{l_0}{2} + dx$, whereas the vertical edge is $r_{EQ} - \delta$. Hence:

$$r_{EQ}^2 = \left(r_{EQ} - \delta\right)^2 + \frac{\left(l_0 + 2dx\right)^2}{4}$$

which finally gets simplified into:

$$r_{EQ} = \frac{\delta}{2} + \frac{\left(l_0 + 2dx\right)^2}{8\delta} \tag{29}$$

and is used to obtain the interfacial radius of curvature r_{EQ} in the simulations. A sample of horizontal stress distribution (i.e. σ_x) is presented on the deformed geometry in Fig. 8 based on the applied deformations of dx (Eq. (26)) and dy (Eq. (28)) and corrosion progress of 1% .

4. Results

The total swelling during the corrosion, which is the sum of the elastic and plastic deformations (Eq. (10)) depends on the scale of the corrosion $\hat{s}$ as well as the properties of the corroded material (Eq. (13)).

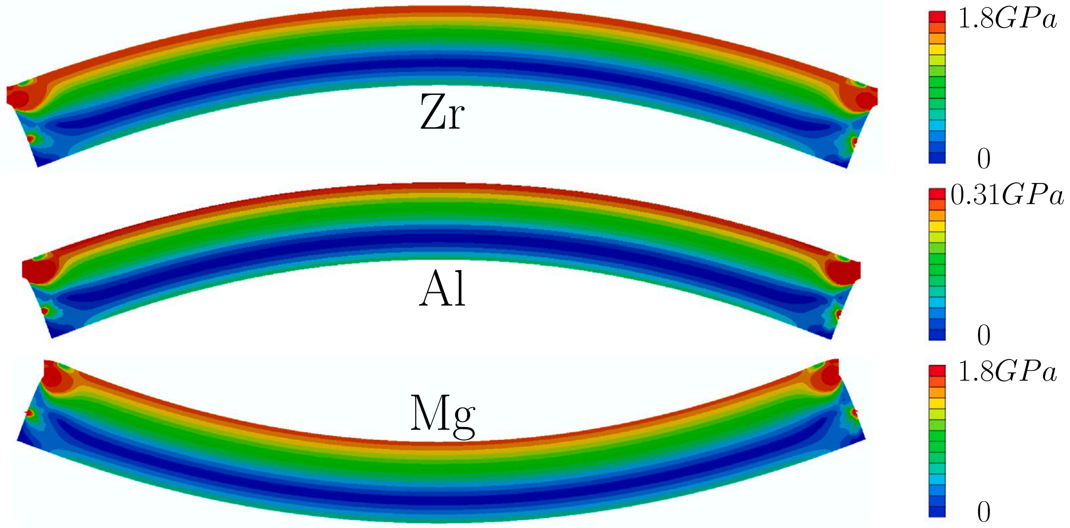

Fig. 8. Sample hypothetical elastic Von Mises distribution (σ) for the three candidate materials of Zirconium Zr, Aluminum Al, and Magnesium Mg, at the corrosion scale of $\hat{s} = 1\%$, #Nodes= 1.3×10^4. The concave bending of the magnesium is due to the oxide shrinkage, and the lower stress value in the aluminum is due to its lower elastic modulus ($E_{Al} \ll E_{Zr}, E_{Mg}$).

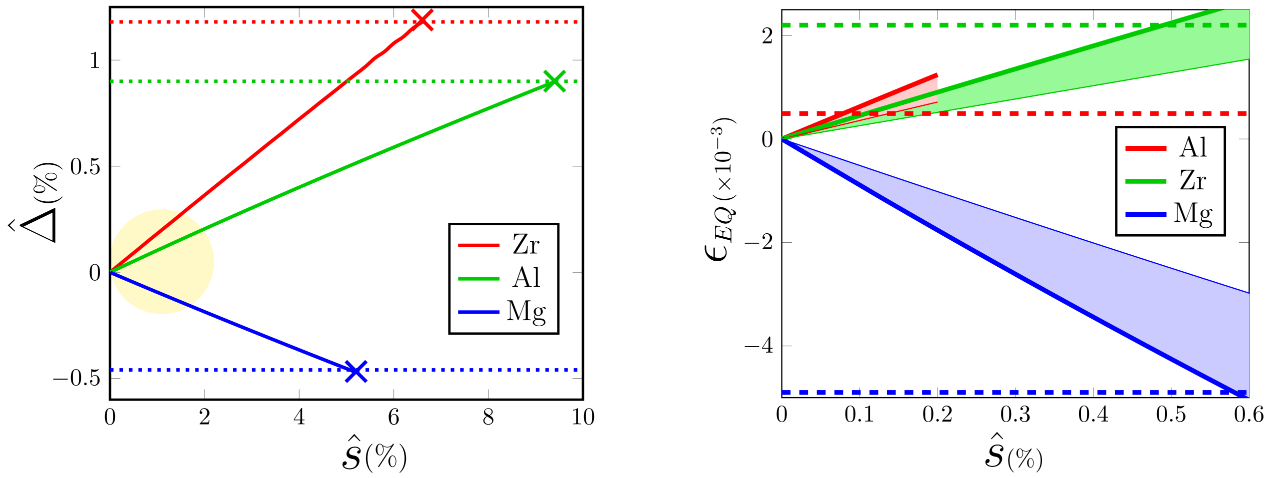

(a) The development of the total swelling $\hat{\Delta}$ within the elastic limit. The initial stage of the corrosion is highlighted in yellow.

(b) Comparison of the evolution of the metallic interfacial strain ϵ_{EQ} in 1D films (thin) versus 2D layers (thick). Dashed lines: yield strain $\epsilon_{y,M}$

Fig. 9. The developments of (a) Normalized total swelling $\hat{\Delta}$ and (b) Interfacial strains ϵ_{EQ}.

In this regard, Fig. 9(a) tracks the normalized swelling $\hat{\Delta}$ of the three investigated metals (Zr, Al, Mg), given their volume-sensitive parameters of Pilling-Bedworth ratio $\hat{R}$ and Poisson's ratios v_O presented in Table 3. Subsequently, one could explore the build-up in the elastic interfacial metallic strain ($\epsilon_{EQ,M} := \epsilon_{EQ}$ from now on) during their infinitesimal corrosion for both 1 and 2 dimensional paradigms, which has been illustrated in Fig. 9(b) for the three candidate materials.

In order to further explore the behavior of the equilibrium scale l_{EQ}, one could extend its development via the assumption of hypothetically remaining elastic beyond the yield limit $\epsilon_{y,M}$, which presumably could extend into the entire corrosion span of $\left[0, \hat{R}\right]$. Figs. 10(a)–10(c) for the 3 candidate materials presented in Table 3.

5. Discussions

The growth behavior in the total swelling, shown in Fig. 9(a), reveals that it correlates to corrosion scale $\hat{s}$ as well as the material properties, including the Pilling-Bedworth ratio R, Poisson's ratio v, and the ratio of elastic moduli $\hat{E}$. Particularly it is noticeable that in the early stages of corrosion ($\hat{s} \to 0$) zirconium Zr swells larger than the aluminum Al (i.e. $\epsilon_{EQ,Al} > \epsilon_{EQ,Zr}$). This can be explained analytically via calculating the sensitivity of the normalized total swelling $\hat{\Delta}$ to the corrosion scale $\hat{s}$, as:

$$\lim_{\hat{s}\to 0} \frac{\partial \hat{\Delta}}{\partial \hat{s}} = \frac{\hat{R}-1}{\hat{R}}$$

which shows sole correlation to the swelling ratio $\hat{R}$, and since $\hat{R}_{Zr} > \hat{R}_{Al}$, the zirconium gets a faster growth during the instigation of corrosion. Performing similar analogy for the equilibrium metallic strain ϵ_{EQ}, the sensitivity to the corrosion scale $\hat{s}$ is obtained as:

$$\lim_{\hat{s}\to 0} \frac{\partial \epsilon_{EQ}}{\partial \hat{s}} = \hat{E}\,\frac{\hat{R}-1}{\hat{R}}$$

which shows a predominant direct correlation with the ratio of the elastic moduli $\hat{E}$ (i.e. $\hat{E}_{Al} > \hat{E}_{Zr}$) and hence the material with higher $\hat{E}$ grows faster, as shown in Fig. 9(b). As well, is evident in this figure that

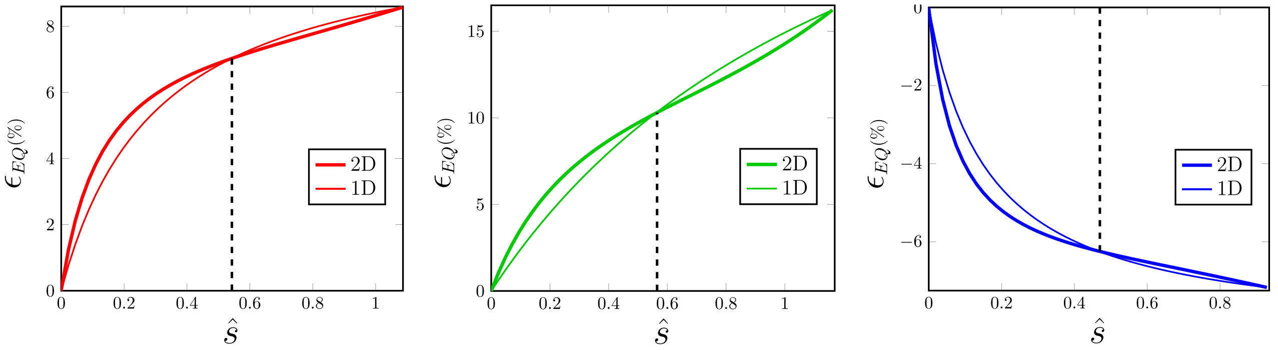

(a) Aluminum Al (b) Zirconium Zr (c) Magnesium Mg

Fig. 10. The hypothetical strain development ϵ_M (beyond the yield strain $\epsilon_{y,M}$) for the 3 candidate materials of (a) Aluminum (b) Zirconium and (c) Magnesium, versus the normalized corrosion scale $\hat{s}$, both in 1D (thin) and 2D (thick) developments.

the 2D corrosion scheme shows a sharper rise (or fall when $\hat{R} < 1$) than the 1D counterpart. The underlying reason is that in 1D development, all the materials deform identically with the interface, while in the 2D case the zones further away from the interface relax and the interface carries more stress in return.

It is obvious that through the progress of the corrosion from the initiation (i.e. $\hat{s} \to 0$) until the end (i.e. $\hat{s} \to \hat{R}$), the equilibrium scale moves from l_0 to $\hat{R}l_0$ ($\hat{R} > 1$: growth, $\hat{R} < 1$: shrink). While such extents are discernible from Equation (8), one could verify them in $2D$ development as well. In the initial stage the coefficients will be:

$$\begin{cases} \lim\limits_{\hat{s}\to 0} A_2 = \dfrac{G_O}{2}\hat{h}\hat{R} \\ \lim\limits_{\hat{s}\to 0} A_1 = -\dfrac{G_O\hat{R}l_0}{2}\hat{h} \\ \lim\limits_{\hat{s}\to 0} A_0 = -2E_O s^2\left(\hat{h}\hat{G}\hat{R}\right)\hat{h} \end{cases}$$

which gets simplified into:

$$G_M h_0\left(l_{EQ}^2 - l l_{EQ}\right) - \left(\frac{1}{\hat{R}}\left(l_{EQ}^2 - l_0 l_{EQ}\right) + 4E_O h_0^2\right) s = 0$$

and in the limit of $\hat{s} \to 0$ it yields to: $l_{EQ} = l_0$✓. As well, on the verge of full corrosion ($\hat{s} \to \hat{R}$), there is only oxide left ($\hat{h} \to 0$) hence:

$$\begin{cases} \lim_{\hat{s}\to\hat{R}} A = \dfrac{G_O}{2}\hat{E} \\ \lim_{\hat{s}\to\hat{R}} B = -\dfrac{G_O\hat{R}l_0}{2}\hat{E} \\ \lim_{\hat{s}\to\hat{R}} C = 0 \end{cases}$$

which gets simplified into:

$$l_{EQ}^2 - \hat{R}l_0 l_{EQ} = 0$$

and yields: $l_{EQ} = \hat{R}l_0$✓. Such sharing the common initial and final equilibrium scales l_{EQ} between $1D$ and $2D$ frameworks is additionally obvious in the behavior of equilibrium strain ϵ_{EQ} in Figs. 10(a)–10(c). Regarding the decelerating-accelerating behavior (curving down and later up for Zr, Al) in the equilibrium interfacial strain ϵ_{EQ}, it is the result of competition between the metal (i.e. smaller when $\hat{R} > 1$) and oxide (i.e. larger when $\hat{R} > 1$). Hence, in the very early stage ($\hat{s} \to 0$) and very late stages ($\hat{s} \to \hat{R}$) of the full corrosion, one medium is significantly weaker compared to the other (oxide in the beginning and metal in the end). Therefore, the 2D framework, which carries higher sensitivity due to stress concentration there will be a sharper variation compared to the 1D framework. However in the middle, particularly at $\hat{s} \approx \frac{\hat{R}}{2}$, both metal and oxide media are competitive relative to each other, and therefore the equilibrium scale l_{EQ} has the least sensitivity to the progress of the corrosion $\hat{s}$.

While the bending of the components due to corrosion has been explored before Zhao and Huntz (1984), one could use the obtained radius of curvature to correlate the modeling framework with the numerical simulations, where the radius of curvature can be calculated from two different perspectives.

The formed radius of curvature r_M in both modeling and simulations, which are obtained in Eqs. (24) and (29) versus the scale of corrosion $\hat{s}$, are compared against each other in Fig. 11, where a substantial agreement is obvious. In this figure the expansion during the metal-to-oxide transition forms convex geometry (i.e. $r_M > 0$, for Zr, Al) while the shrinkage leads to concave form (i.e. $r_M < 0$ for Mg).

The bending and formation of curvature in both oxide and metal ultimately can lead to failure and delamination in both media. One could interpret curvature-induced stresses from the swelling, similar to curvature formed from an external moment in flexural mode. Here, we focus on the metal part, as it experiences more curvature than the oxide. Assuming that neutral axis remains almost in the center (i.e. small curvature) due to very small difference in the interfacial l_{EQ} and the bottom l_B boundaries, the maximum generated strain ϵ in the material cross-section would be:

$$\epsilon = \frac{1}{2}\frac{l_{EQ} - l_B}{l_B}$$

where the coefficient of $\frac{1}{2}$ is due to dividing the flexural cross-section into compression and tension zones. The failure occurs when the generated strain meet the yield value $\epsilon_{y,M}$, and simplification leads to:

$$l_{EQ} = l_B\left(1 + 2\epsilon_{y,M}\right)$$

therefore, one could calculate the interfacial radius of curvature causing the onset of yielding, as:

$$r_{EQ} \approx \frac{1 + 2\epsilon_{y,M}}{2\epsilon_{y,M}}\left(h_0 - \frac{s}{\hat{R}}\right)$$

which means that for higher amount of yield strain, shorter radius of curvature is required to reach failure. As well, more progress of corrosion (s ↑) forms more curvature (i.e. less radius r_{EQ} ↓), which ultimately leads to delamination and spalling, which is particularly more feasible in the interface of the oxide and metal due to weaker chemical bonding. The quantification of such delamination based on the state of corrosion is the subject of our next study.

From Fig. 9(b) and Eq. (8), one could further compare the sensitivity of the formed stress $\hat{\sigma}_M$ with respect to these parameters to find the dominant effect. Hence:

$$\begin{cases} \lim\limits_{\hat{s}\to 0}\dfrac{\partial\hat{\sigma}_M}{\partial\hat{E}} \approx \dfrac{\hat{s}}{\epsilon_{y,M}}\left(\dfrac{\left(\hat{R}-\hat{s}\right)\left(\hat{R}-1\right)}{\left(\hat{R}+\left(\hat{E}-1\right)\hat{s}\right)^2}\right) \\ \lim\limits_{\hat{s}\to 0}\dfrac{\partial\hat{\sigma}_M}{\partial\hat{R}} \approx \dfrac{\hat{s}\hat{E}}{\epsilon_{y,M}}\left(\dfrac{1+\left(\hat{E}-1\right)\hat{s}}{\left(\hat{R}+\left(\hat{E}-1\right)\hat{s}\right)^2}\right) \end{cases} \tag{30}$$

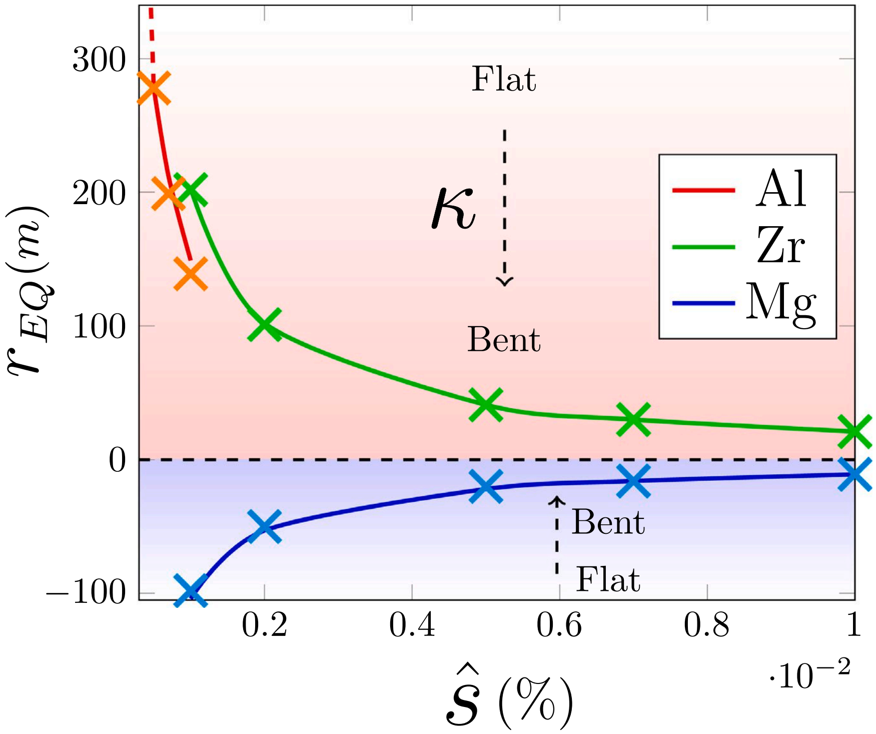

Fig. 11. The evolution of the metallic radius of curvature r_M versus the corrosion scale $\hat{s}$ for the candidate materials of zirconium Zr, aluminum Al and magnesium Mg. The solid lines represent the constitutive modeling and the crosses (×) signify the simulation results. As well, the red zone is the convex (outward) deformation while the blue zone shows forming the concave (inward) geometry.

where comparison yields a quadratic in terms of $\hat{R}$ as:

$$\hat{R}^2 - (\hat{s}+1)\,\hat{R} + \left(\hat{s} + \hat{E} + \hat{E}^2\hat{s} - \hat{E}\hat{s}\right) = 0$$

Particularly in the initiation stage of corrosion (i.e. $\hat{s} \to 0$) one gets:

$$\hat{R} = \frac{1}{2}\left\{1 \pm \sqrt{1 - 4\hat{E}}\right\}$$

Since almost always $\hat{E} > \frac{1}{4}$, there is no solution, which means that the sensitivity of the normalized metallic stress is always higher to the ratio of elastic moduli $\hat{E}$ than the swelling ratio $\hat{R}$.

Needless to mention that the verifications for both modeling and simulations were performed assuming the hypothetical elastic (i.e. linear) behavior, which extends beyond the yielding limit. As well, similar to the linear distribution of the shear stress in the interface, the variation of the stress profile in the vertical direction was assumed to be linear. The developed model could be complemented with the addition of plasticity, fracture behavior and inclusion of the other corrosion-contributing mechanisms such as side corrosion, and metal diffusion where the amount of formed stress is negligible.

Finally, while the evidence for the current theoretical findings from the literature is very rare, a complementary experimental investigation would be necessary, particularly since this study considers sole effect of oxygen diffusion (as opposed to metal diffusion) which generates the maximum amount of stress. Furthermore, this work merely has explored the mechanical aspect of corrosion, which is a reaction-induced internal drive for swelling, and generation of mismatch, and other factors such as thermo-mechanics, creep deformation in high temperatures, transient behavior and particularly stress-assisted diffusion, passivation, formation of side-products (i.e. hydroxides, phase transformation, etc.) are to be studied separately.

6. Conclusions

A new closed-form corrosion state-dependent constitutive model has been developed for predicting the nonlinear swelling-induced accumulation of mismatch compressive/tensile strains/stresses. Utilizing the natural volume difference during the metal-to-oxide transition, we quantify the balanced equilibrium scale analytically in the interface of binary composite, and the following swelling due to elastic and corrosion (i.e. plastic) events, which has been derived for in both 1D (thin oxide film) and 2D (thick oxide layer). The formed radius of curvature has been used for verification with the finite element simulations. Furthermore, performing hypothetical elastic derivations for the entire corrosion span we have explained the non-linear behavior in the rate of strain accumulation, particularly in the beginning and end of corrosion. Consequently, the dominant material parameter for the establishment of the metallic strain, total swelling, and metallic stress has been determined. The developed framework could be useful for the design and materials selection process and maintenance of the components in corrosion-sensitive environments, particularly those involving large swellings.

CRediT authorship contribution statement

Asghar Aryanfar: Writing – review & editing, Writing – original draft, Visualization, Validation, Software, Methodology, Formal analysis, Data curation, Conceptualization. **Semih Can:** Software, Investigation. **Umut Ureyen:** Validation, Methodology. **William Goddard III:** Project administration.

Declaration of competing interest

The authors declare that they have no known competing financial interests or personal relationships that could have appeared to influence the work reported in this paper.

Data availability

Data will be made available on request.

References

Abadias, Grégory, Chason, Eric, Keckes, Jozef, Sebastiani, Marco, Thompson, Gregory B., Barthel, Etienne, Doll, Gary L., Murray, Conal E., Stoessel, Chris H., Martinu, Ludvik, 2018. Stress in thin films and coatings: Current status, challenges, and prospects. J. Vac. Sci. Technol. A: Vac. Surf. Films 36 (2), 020801.

Abawi, Ahmad T., 2004. The bending of bonded layers due to thermal stress. Hughes Research Laboratories, Malibu, CA.

Aryanfar, Asghar, Tallis, El, Rahman, Abdel, Marian, Jaime, 2022. Coupling the corrosion-and pressure-assisted stress buildup within the zirconium in PWR pipes. JOM 1–12.

Atrens, Andrej, Shi, Zhiming, Mehreen, Syeda U., Johnston, Sean, Song, Guang-Ling, Chen, Xianhua, Pan, Fusheng, 2020. Review of Mg alloy corrosion rates. J. Magnes. Alloy. 8 (4), 989–998.

Bedworth, R.E., Pilling, N.B., 1923. The oxidation of metals at high temperatures. J. Inst. Met. 29 (3), 529–582.

Birks, Neil, Meier, Gerald H., Pettit, Frederick S., 2006. Introduction to the High Temperature Oxidation of Metals. Cambridge University Press.

Birnie, J., Craggs, C., Gardiner, D.J., Graves, P.R., 1992. Ex situ and in situ determination of stress distributions in chromium oxide films by Raman microscopy. Corros. Sci. 33 (1), 1–12.

Broomfield, John P., 2023. Corrosion of Steel in Concrete: Understanding, Investigation and Repair. Crc Press.

Callister Jr., William D., Rethwisch, David G., 2020. Callister's Materials Science and Engineering. John Wiley and Sons.

Causey, Rion A., Cowgill, Donald F., Nilson, Robert H., 2005. Review of the Oxidation Rate of Zirconium Alloys. Report, Sandia National Laboratories.

Chen, Gang, Liu, Shuying, Huang, Chao, Ma, Yuan, Li, Ying, Zhang, Baicheng, Gao, Lei, Zhang, Bowei, Wang, Pei, Qu, Xuanhui, 2022. In-situ phase transformation and corrosion behavior of TiNi via LPBF. Corros. Sci. 203, 110348.

Chen, Q.S., Liu, C.H., Long, J.P., Wang, J., Zhang, R.Q., Yang, H.Y., Zhang, W., Yao, F.Y., Zhao, S., Zhang, Q., 2019. Microstructure and corrosion characteristics of CrCuFeMoNi HEA coatings with different compositions in high-temperature and high-pressure water. Mater. Res. Express 6 (8), 086511.

Choi, Byoung-Ho, Chudnovsky, Alexander, Sehanobish, Kalyan, 2007. Stress corrosion cracking in plastic pipes: observation and modeling. Int. J. Fract. 145 (1), 81–88.

Chou, Kuo-Chih, Luo, Qun, Li, Qian, Zhang, Jie-Yu, 2014. Influence of the density of oxide on oxidation kinetics. Intermetallics 47, 17–22.

Clarke, D.R., 2003. The lateral growth strain accompanying the formation of a thermally grown oxide. Acta Mater. 51 (5), 1393–1407.

Cox, B., 2005. Some thoughts on the mechanisms of in-reactor corrosion of zirconium alloys. J. Nucl. Mater. 336 (2), 331–368.

Cramer, Stephen D., Covino Jr., Bernard S., Moosbrugger, Charles, Sanders, Bonnie R., Anton, Gayle J., Hrivnak, Nancy, Kinson, Jill, Polakowski, Carol, Muldoon, Kathryn, Henry, Scott D., et al., 2003. ASM Handbook. vol. 13, ASM international Materials Park, Ohio.

De González, Cristina O., García, Eduardo A., 1990. Determination of the diffusion coefficients of oxygen in zirconium by means of XPS. Appl. Surf. Sci. 44 (3), 211–219.

Dillard, David A., 2002. Fundamentals of stress transfer in bonded systems. Adhes. Sci. Eng. 1–44.

DiMeglio, John L., Bartlett, Bart M., 2017. Interplay of corrosion and photocatalysis during nonaqueous benzylamine oxidation on cadmium sulfide. Chem. Mater. 29 (17), 7579–7586.

Dong, Enci, Cao, Sida, Zhang, Ruiyuan, Chen, Li, Tao, Wenquan, 2024. A one-dimensional numerical model of carbon corrosion in catalyst layers of proton exchange membrane fuel cells. Electrochim. Acta 144030.

Dong, Xuelin, Fang, Xufei, Feng, Xue, Hwang, Keh-Chih, 2013. Diffusion and stress coupling effect during oxidation at high temperature. J. Am. Ceram. Soc. 96 (1), 44–46.

Drozdov, A.D., Christiansen, J. deClaville, 2016. Swelling-induced bending of bilayer gel beams. Compos. Struct. 153, 961–971.

Duck, Graham, Renaud, Guillaume, et al., 1999. The mechanical load transfer into a distributed optical fiber sensor due to a linear strain gradient: embedded and surface bonded cases. Smart Mater. Struct. 8 (2), 175.

Dwivedi, Deepak, Lepková, Kateřina, Becker, Thomas, 2017. Carbon steel corrosion: a review of key surface properties and characterization methods. RSC Adv. 7 (8), 4580–4610.

El Maaddawy, Tamer, Soudki, Khaled, 2007. A model for prediction of time from corrosion initiation to corrosion cracking. Cem. Concr. Compos. 29 (3), 168–175.

El-Sherik, A.M., 2017. Trends in Oil and Gas Corrosion Research and Technologies: Production and Transmission. Woodhead Publishing.

Eliaz, Noam, 2019. Corrosion of metallic biomaterials: A review. Materials 12 (3), 407.

Eliseev, Artem A., Chumakov, Andrei P., Petukhov, Dmitry I., Eliseev, Andrei A., 2024. Temperature controlled swelling of graphene oxide for switchable dehumidification membranes. J. Membr. Sci. 690, 122213.

Evans, H.E., Huntz, A.M., 1994. Methods of measuring oxidation growth stresses. Mater. High Temp. 12 (2–3), 111–117.

Fatima, Tasnim, Arab, Nasrin, Zemskov, Evgeny P., Muntean, Adrian, 2011. Homogenization of a reaction diffusion system modeling sulfate corrosion of concrete in locally periodic perforated domains. J. Engrg. Math. 69.

Fettre, D., Bouvier, Salima, Favergeon, J., Kurpaska, L., 2015. Residual stresses in high temperature corrosion of pure zirconium using elasto-viscoplastic model: Application to the deflection test in monofacial oxidation. Appl. Surf. Sci. 357, 777–786.

Forsberg, K., Limback, M., Massih, A.R., 1995. A model for uniform zircaloy clad corrosion in pressurized water reactors. Nucl. Eng. Des. 154 (2), 157–168.

Freund, Lambert Ben, Suresh, Subra, 2004. Thin Film Materials: Stress, Defect Formation and Surface Evolution. Cambridge University Press.

Gaidis, James M., 2004. Chemistry of corrosion inhibitors. Cem. Concr. Compos. 26 (3), 181–189.

Ganser, Markus, Hildebrand, Felix E., Klinsmann, Markus, Hanauer, Matthias, Kamlah, Marc, McMeeking, Robert M., 2019. An extended formulation of butler-volmer electrochemical reaction kinetics including the influence of mechanics. J. Electrochem. Soc. 166 (4), H167.

Gholami, Mahboobe, Hoseinpoor, M., Moayed, Mohammad Hadi, 2015. A statistical study on the effect of annealing temperature on pitting corrosion resistance of 2205 duplex stainless steel. Corros. Sci. 94, 156–164.

Goedjen, John G., Shores, David A., Stout, James H., 1997. In-situ strain measurements in the Ni/NiO system during high temperature oxidation. Mater. Sci. Eng.: A 222 (1), 58–69.

Gwinner, Benoit, Balbaud-Célérier, F., Fauvet, Pierre, Gruet, Nathalie, Laghoutaris, Pierre, Miserque, Frédéric, Robin, Raphael, 2022. A step towards a better understanding of corrosion of zirconium in nitric acid with additions of fluorine: Focus on the role of the presence of an initial oxide film. Corros. Sci. 201, 110284.

Hillner, Edward, 1977. Corrosion of zirconium-base. Zircon. Nucl. Ind. 633, 211.

Huang, Xu, Yang, Hui, Liang, Wentao, Raju, Muralikrishna, Terrones, Mauricio, Crespi, Vincent H., Van Duin, Adri C.T., Zhang, Sulin, 2013. Lithiation induced corrosive fracture in defective carbon nanotubes. Appl. Phys. Lett. 103 (15), 153901.

Huntz, A.M., Calvarin Amiri, G., Evans, H.E., Cailletaud, G., 2002. Comparison of oxidation-growth stresses in NiO film measured by deflection and calculated using creep analysis or finite-element modeling. Oxid. Met. 57, 499–521.

Huntz, A.M., Hou, P.Y., Molins, Régine, 2007. Study by deflection of the oxygen pressure influence on the phase transformation in alumina thin films formed by oxidation of Fe3Al. Mater. Sci. Eng.: A 467 (1–2), 59–70.

Jacques, Patrick, Lefebvre, Florence, Lemaignan, Clement, 1999. Deformation corrosion interactions for Zr alloys during I SCC crack initiation: Part II: Localised stress and strain contributions. J. Nucl. Mater. 264 (3), 249–256.

Jafarzadeh, Siavash, Chen, Ziguang, Bobaru, Florin, 2019. Computational modeling of pitting corrosion. Corros. Rev. 37 (5), 419–439.

Khasanova, A.R., 2022. Corrosion cracking under main pipelines stress. J. Phys.: Conf. Ser. 2176 (1), 012051.

Kimura, M., Totsuka, N., Kurisu, T., Amano, K., Matsuyama, J., Nakai, Y., 1989. Sulfide stress corrosion cracking of line pipe. Corrosion 45 (4), 340–346.

Knittel, Donald R., Bronson, Arturo, 1984. Pitting corrosion on zirconium: a review. Corrosion 40 (1), 9–14.

Kozlovskiy, A.L., Zdorovets, M.V., 2019. Synthesis, structural, strength and corrosion properties of thin films of the type CuX (X=Bi, Mg, Ni). J. Mater. Sci., Mater. Electron. 30, 11819–11832.

Kurpaska, L., Favergeon, Jerome, Grosseau-Poussard, Jean-Luc, Lahoche, L., Moulin, G., 2016. In-situ stress analysis of the Zr/ZrO2 system as studied by Raman spectroscopy and deflection test in monofacial oxidation techniques. Appl. Surf. Sci. 385, 106–112.

Kurpaska, L., Favergeon, Jerome, Lahoche, L., Moulin, G., 2018. On the determination of growth stress during oxidation of pure zirconium at elevated temperature. Appl. Surf. Sci. 446, 27–35.

Le Saux, M., Guilbert, T., Brachet, J.C., 2018. An approach to study oxidation-induced stresses in Zr alloys oxidized at high temperature. Corros. Sci. 140, 79–91.

Li, Yusha, Ge, Changchun, Liu, Yanhong, Li, Guangbin, Dong, Xiaoxu, Gu, Zongxing, Zhang, Yingchun, 2022. Influencing factors and mechanism of iodine-induced stress corrosion cracking of zirconium alloy cladding: A review. Int. J. Miner. Met. Mater. 29 (4), 586–598.

Li, Meishuan, Li, Tiefan, Gao, Wei, Liu, Zhenyu, 1999. Determination of oxide growth stress by a novel deflection method. Oxid. Met. 51 (5–6), 333–351.

Li, Shu-Xin, Yu, Shu-Rong, Zeng, Hai-Long, Li, Jian-Hua, Liang, Rui, 2009. Predicting corrosion remaining life of underground pipelines with a mechanically-based probabilistic model. J. Pet. Sci. Eng. 65 (3–4), 162–166.

Lin, Naiming, Liu, Qiang, Zou, Jiaojuan, Li, Dali, Yuan, Shuo, Wang, Zhihua, Tang, Bin, 2017. Surface damage mitigation of Ti6Al4V alloy via thermal oxidation for oil and gas exploitation application: characterization of the microstructure and evaluation of the surface performance. RSC Adv. 7 (22), 13517–13535.

Liu, Chao, Kelly, Robert G., 2019. A review of the application of finite element method (FEM) to localized corrosion modeling. Corrosion 75 (11), 1285–1299.

Ma, Haonan, Zhang, Weidong, Wang, Yao, Ai, Yibo, Zheng, Wenyue, 2023. Advances in corrosion growth modeling for oil and gas pipelines: A review. Process. Saf. Environ. Prot. 171, 71–86.

Mahesh, B.V., Raman, R.K. Singh, 2014. Role of nanostructure in electrochemical corrosion and high temperature oxidation: a review. Met. Mater. Trans. A 45, 5799–5822.

Marcus, Philippe, 2011. Corrosion Mechanisms in Theory and Practice. CRC Press.

Mermoux, Michel, Duriez, Christian, 2021. Raman imaging in corrosion science: High-temperature oxidation of the zirconium alloys used in the nuclear industry as an example. J. Raman Spectrosc. 52 (12), 2131–2159.

Mohanty, S., Majumdar, S., Natesan, K., 2012. A review of stress corrosion cracking/fatigue modeling for light water reactor cooling system components. Argonne, IL: Nucl. Eng. Div. Argonne Natl. Lab..

Mojdehi, Ahmad R., Holmes, Douglas P., Dillard, David A., 2017. Friction of extensible strips: an extended shear lag model with experimental evaluation. Int. J. Solids Struct. 124, 125–134.

Motta, Arthur T., Yilmazbayhan, Aylin, da Silva, Marcelo J. Gomes, Comstock, Robert J., Was, Gary S., Busby, Jeremy T., Gartner, Eric, Peng, Qunjia, Jeong, Yong Hwan, Park, Jeong Yong, 2007. Zirconium alloys for supercritical water reactor applications: Challenges and possibilities. J. Nucl. Mater. 371 (1), 61–75.

Noden, J.D., Knights, C.J., Thomas, M.W., 1968. Growth of austenitic stainless steels oxidised in carbon and oxygen bearing gases. Br. Corros. J. 3 (1), 47–55.

Panchenko, Yu M., Marshakov, A.I., 2016. Long-term prediction of metal corrosion losses in atmosphere using a power-linear function. Corros. Sci. 109, 217–229.

Parise, M., Sicardy, O., Cailletaud, G., 1998. Modelling of the mechanical behavior of the metal–oxide system during Zr alloy oxidation. J. Nucl. Mater. 256 (1), 35–46.

Pemsler, J. Paul, 1958. Diffusion of oxygen in zirconium and its relation to oxidation and corrosion. J. Electrochem. Soc. 105 (6), 315–322.

Pezzulla, Matteo, Smith, Gabriel P., Nardinocchi, Paola, Holmes, Douglas P., 2016. Geometry and mechanics of thin growing bilayers. Soft Matter 12 (19), 4435–4442.

Preuss, Michael, 2021. A review of early findings within the collaborative research programme MUZIC: Mechanistic understanding of zirconium corrosion. In: Zirconium in the Nuclear Industry: 19th International Symposium. ASTM International.

Reyes, Michael, Aryanfar, Asghar, Baek, Sun Woong, Marian, Jaime, 2018. Multilayer interface tracking model of zirconium clad oxidation. J. Nucl. Mater. 509, 550–565.

Rhines, F.N., Wolf, J.S., 1970. The role of oxide microstructure and growth stresses in the high-temperature scaling of nickel. Met. Trans. 1, 1701–1710.

Roy, C., Burgess, B., 1970. A study of the stresses generated in zirconia films during the oxidation of zirconium alloys. Oxid. Met. 2 (3), 235–261.

Ruan, J.L., Pei, Yongmao, Fang, Daining, 2012. Residual stress analysis in the oxide scale/metal substrate system due to oxidation growth strain and creep deformation. Acta Mech. 223 (12), 2597–2607.

Ruan, J.L., Pei, Yongmao, Fang, Daining, 2013. On the elastic and creep stress analysis modeling in the oxide scale/metal substrate system due to oxidation growth strain. Corros. Sci. 66, 315–323.

Sander, G., Tan, J., Balan, P., Gharbi, O., Feenstra, D.R., Singer, L., Thomas, S., Kelly, R.G., Scully, John R., Birbilis, Nick, 2018. Corrosion of additively manufactured alloys: a review. Corrosion 74 (12), 1318–1350.

Saunders, S.R.J., Evans, H.E., Li, M., Gohil, D.D., Osgerby, S., 1997. Oxidation growth stresses in an alumina-forming ferritic steel measured by creep deflection. Oxid. Met. 48, 189–200.

Seddiqi, Hadi, Sadatshojaie, Ali, Vaferi, Behzad, Yahyazadeh, Ehsan, Salehi, Afshin, Wood, David A., 2020. Mathematical model for iron corrosion that eliminates chemical potential parameters. Chin. J. Chem. Eng. 28 (2), 603–612.

Singh, Chandra Veer, 2018. 2.7 Micromechanics of Damage Evolution in Laminates. Elsevier.

Singh, Raghuvir, Dahotre, Narendra B., 2007. Corrosion degradation and prevention by surface modification of biometallic materials. J. Mater. Sci., Mater. Med. 18, 725–751.

Song, Wei, Liu, Xuesong, Wang, Ping, Liu, Yong, Berto, Filippo, 2022. Strength mismatch effect on residual stress of 10CrNi3MoV steel considering the back-chipping process. Int. J. Press. Vessels Pip. 195, 104570.

Stafiej, Janusz, Di Caprio, Dung, Bartosik, Łukasz, 2013. Corrosion-passivation processes in a cellular automata based simulation study. J. Supercomput. 65, 697–709.

Stoney, George Gerald, 1909. The tension of metallic films deposited by electrolysis. Proc. R. Soc. Lond. Ser. A, Contain. Pap. A Math. Phys. Character 82 (553), 172–175.

Stout, J.H., Shores, D.A., Goedjen, J.G., Armacanqui, M.E., 1989. Stresses and cracking of oxide scales. Mater. Sci. Eng.: A 120, 193–197.

Subramaniam, Anandh, Ramakrishnan, N., 2003. Analysis of thin film growth using finite element method. Surf. Coat. Technol. 167 (2–3), 249–254.

Sun, Xiangyang, Gong, Feng, Hao, Menglong, Wu, Lei, Yin, Chunyu, Sun, Zhipeng, Xiao, Rui, 2022. Enhanced thermal transport and corrosion resistance by coating vertically-aligned graphene on zirconium alloy for nuclear reactor applications. Appl. Surf. Sci. 582, 152484.

Was, Gary S., Ashida, Yugo, Andresen, Peter L., 2011. Irradiation-Assisted Stress Corrosion Cracking. Walter de Gruyter.

Wilczynska, Kamila, Bono, Matthew, Le Boulch, David, Fregonese, Marion, Chabretou, Valérie, Mozzani, Nathanael, Barbie, Laureline, 2019. Development and validation of a new experimental device for studies of iodine stress corrosion cracking of zirconium alloys. In: 19th International Conference on Environmental Degradation of Materials in Nuclear Power Systems-Water Reactors.

Xu, Chunhua, Gao, Wei, 2000. Pilling-Bedworth ratio for oxidation of alloys. Mater. Res. Innov. 3 (4), 231–235.

Yang, Fuqian, 2023. Stress-induced change of ground-state energy of a semiconductor core-shell nanocrystal: Effect of mismatch strain and hydrostatic pressure. Phys. Lett. A 471, 128788.

Yin, Z. Fa, Feng, Y.R., Zhao, W.Z., Bai, Z.Q., Lin, G.F., 2009. Effect of temperature on CO2 corrosion of carbon steel. Surf. Interface Anal.: Int. J. Devoted To Dev. Appl. Tech. Anal. Surfaces Interfaces Thin Films 41 (6), 517–523.

Young, David John, 2008. High Temperature Oxidation and Corrosion of Metals. vol. 1, Elsevier.

Zaimovskii, A.S., 1978. Zirconium alloys in nuclear power. Sov. At. Energy 45 (6), 1165–1168.

Zhang, X.Y., Shi, M.H., Li, C., Liu, N.F., Wei, Y.M., 2007. The influence of grain size on the corrosion resistance of nanocrystalline zirconium metal. Mater. Sci. Eng.: A 448 (1–2), 259–263.

Zhang, Jinsong, Wang, Jinyang, Tang, Yunlong, Qu, Zhe, Feng, Xue, 2023. A curvature-dependent chemo-mechanical coupling model for two-dimensional oxidation on the curved surface. Int. J. Solids Struct. 112363.

Zhang, Weiwei, Wu, Haowei, 2023. Numerical analysis on the thermal mismatch stress of quasi-isotropic strand with square cross section during cool-down. Cryogenics 131, 103666.

Zhao, Kejie, Cui, Yi, 2016. Understanding the role of mechanics in energy materials: A perspective. Extrem. Mech. Lett. 9, 347–352.

Zhao, J.G., Huntz, A.M., 1984. Theoretical analysis of the deflection test used in single-surface oxidation of metallic samples. J. Mater. Sci. 19, 3166–3172.

Zhao, Ying, Stein, Peter, Bai, Yang, Al-Siraj, Mamun, Yang, Yangyiwei, Xu, Bai-Xiang, 2019. A review on modeling of electro-chemo-mechanics in lithium-ion batteries. J. Power Sources 413, 259–283.

Zhao, Yan, Wang, Yuan, Li, Xin, Zhang, Weina, Tang, Shuai, Liu, Zhenyu, 2018. Effects of plastic straining on the corrosion resistance of TRIP-aided lean duplex stainless steels. J. Mater. Sci. 53.